Surface Science 688 (2019) 63–68

Contents lists available at ScienceDirect

Surface Science

journal homepage: www.elsevier.com/locate/susc

Oxygen dissolution and surface oxide reconstructions on Nb(100)

R. Darren Veit, Natalie A. Kautz, Rachael G. Farber, S.J. Sibener*

The James Franck Institute and Department of Chemistry, The University of Chicago, 929 E. 57th Street, Chicago, IL 60637, USA

ARTICLE INFO

Keywords:
Oxygen dissolution
STM
AES
Surface oxide
Niobium
SRF cavities

ABSTRACT

The ever-present native oxide layer on niobium plays a fundamental role in the performance of Nb superconducting radio frequency (SRF) cavities for particle accelerators and light sources. Using Nb(111) and Nb(100) as model systems, oxygen dissolution and surface structural evolution as a function of thermal treatments in ultrahigh vacuum (UHV) were studied using combined Auger electron spectroscopy (AES) and scanning tunneling microscopy (STM), providing novel, real space information regarding the complex evolution of the Nb surface oxide. The surface crystallographic orientation was shown to influence oxide surface structure; Nb(111) displayed disordered surface oxide domains while Nb(100) was comprised of well-ordered, $(n \times 1)$-O domains. The temperature-dependent dissolution of the native oxide layer on Nb(100) was characterized to ascertain the energetics for oxygen dissolution, and evolution of the surface oxide superlattice structure following thermal annealing was observed with STM. By understanding the kinetic behavior of oxygen dissolution during thermal annealing and subsequent structural evolution of the Nb$(n \times 1)$-O superlattice on Nb(100), a more thorough understanding of the complex interactions driving chemical composition and cavity surface structure under Nb SRF cavity processing and operating conditions may be understood.

1. Introduction

Niobium (Nb) is the current material of choice for superconducting radio frequency (SRF) cavities for particle accelerators due to its ultra-low surface resistance (R_s) and high cavity quality factor (Q) at operating temperatures $\lesssim$ 2 K [1–4]. To ensure optimal SRF cavity performance, much work has been done to characterize factors impacting SRF cavity performance and to improve cavity preparation techniques [5–9]. It was determined through these studies that Nb superconductivity is dependent on the chemical and structural properties of the first 40–100 nm of the interior cavity surface [1]. Under actual Nb SRF cavity fabrication and operating conditions, an ever-present native oxide layer covers the entirety of the Nb surface, and the surface structure and chemical identity of the oxide layer directly effects SRF cavity performance. During electrochemical polishing procedures that remove $\approx$ 120 μm of the cavity surface, the Nb oxide layer is stripped, allowing the rapid incorporation of hydrogen into the Nb cavity [7,10,11]; immediately following electrochemical polishing, the native oxide reforms, effectively trapping the absorbed hydrogen. This incorporated hydrogen segregates to the surface of Nb cavities forming Nb hydride features that quench superconducting behavior, and significant work is being done to identify beneficial dopants to inhibit the growth of harmful Nb hydride species [2,12,13]. In addition to the formation and removal of the native oxide allowing the incorporation of harmful or beneficial chemical dopants, the quality of the native oxide directly effects the formation of uniform thin films of high efficiency alloys, such as Nb_3Sn [14]. Nb_3Sn has a lower R_s than Nb as a function of temperature, resulting in higher Q factors at a given temperature, thus improving the performance of particle accelerator facilities [15–17]. Results suggesting the importance of the native oxide characteristics and quality influencing Nb_3Sn growth further supports the continued interest in understanding the behavior of Nb oxide under fabrication and operating conditions. It is, therefore, imperative to obtain a fundamental understanding of the complex interplay between surface and near surface chemical species and evolution of the native Nb oxide surface structure under various fabrication and operating conditions.

Particular emphasis on elucidating the intermolecular interactions between Nb and impurities such as oxygen, hydrogen, nitrogen, and carbon which significantly influence SRF cavity R_s and Q [2–5,7,8,10–13] is especially relevant. Nb readily binds oxygen, and the oxidation of Nb and subsequent effect on superconductivity is of great interest and has been extensively studied in the past [18–34]. It was determined that bulk oxide films quench superconductivity while thin films of surface oxide do not effect superconducting behavior to such a large degree. In operational SRF cavities, mild baking of the cavities at

* Corresponding author.
E-mail address: s-sibener@uchicago.edu (S.J. Sibener).

https://doi.org/10.1016/j.susc.2019.06.004
Received 12 May 2019; Received in revised form 3 June 2019; Accepted 7 June 2019
Available online 08 June 2019
0039-6028/

100 – 200 °C in vacuum or air has profound effects on cavity performance [1,7,9], and it is necessary to understand the complex surface evolution that occurs during the initial stages of oxidation. The initial stages of Nb oxidation have been investigated using a variety of ultra-high vacuum (UHV) surface science techniques such as Auger electron spectroscopy [20–24,35,36], x-ray photoelectron spectroscopy (XPS) [23,24,30,37], ultra-violet photoelectron spectroscopy (UPS) [23,25,26], electron energy loss spectroscopy (EELS) [18,22,26], mirror electron microscopy [35], and secondary ion mass spectrometry (SIMS) [21,22]. Such studies have revealed complex interactions between oxygen and Nb, and that producing a clean, oxygen-free Nb surface is experimentally extremely difficult [18–23,26,36]. This is due to the high reactivity of Nb to oxygen and a strong preference for oxygen surface segregation. Farrell et al. [20] found that oxygen was detected on the Nb surface using AES at temperatures up to 1900 K, and Nb samples on the order of 1300 K with bulk oxygen concentrations well below the bulk solubility limit still exhibited roughly quarter monolayer surface oxygen coverage. Oxygen removal occurs *via* desorption of oxygen incorporated into NbO and NbO_2 [18,35,38] and begins at temperatures greater than 1900 K in UHV; complete oxygen removal is only achieved at temperatures greater than 2500 K [18,20,21,35,36].

Due to the high reactivity of Nb to oxygen, exposure of a cleaned Nb surface to low pressures of oxygen at room temperature results in oxygen chemisorption [18,21,22] and the subsequent formation of NbO, NbO_2, and Nb_2O_5 oxidic phases [18,21–23,25,26]. The surface oxide layers at atmospheric pressure are comprised of Nb_2O_5, NbO_2, NbO, as well as metal-rich suboxides [39]. The Nb_2O_5 bulk pentoxide is most stable under ambient conditions and is the dominant oxide phase on the surface when present [39]. Removal of Nb_2O_5 is achieved when the sample is annealed in UHV above 600 K; Nb_2O_5 is reduced to NbO_2 and then NbO as oxygen is dissolved in the bulk of the metal [30,37,40]. The morphology of the niobium surface during thermal cleaning and oxidation has been studied in the past with low energy electron diffraction (LEED) [20,29,35,36].

More recently, atomically resolved structures have been observed on Nb(100) [33,34,41–43] and Nb(110) [31,32,44] with scanning tunneling microscopy (STM). On Nb(110), a surface comprised of quasiperiodical features is reported after Ar^+ ion sputtering and annealing between 1200–2200 K in UHV [31,32,44]. An et al. [41] provide a thorough review of the oxygen-induced structures that form on Nb(100). As a result of thermal cleaning in UHV, a (3 × 1)-O structure forms as a result of the epitaxial growth of NbO/Nb above 873 K. A less oxygen-rich (4 × 1)-O structure forms after annealing the (3 × 1)-O structure at 2270 K as a result of oxygen desorption at higher annealing temperatures. While the two ladder structures, (3 × 1)-O and (4 × 1)-O, have been well characterized, no studies have been done investigating the energetics of oxygen dissolution at elevated temperatures relevant to Nb SRF cavity fabrication, nor has the surface evolution of the oxidized surface following thermal annealing been elucidated. To better understand the mechanism for oxygen dissolution of (3 × 1)-O/Nb(100), our study focuses on the atomic-scale structural evolution and kinetics of the (3 × 1)-O structure as a result of oxygen dissolution of the surface oxide layers on Nb(100).

2. Experimental

Niobium single crystals oriented to the (111), (110), and (100) faces with 99.99% purity were obtained from Surface Preparation Laboratory. The crystals were mounted in a custom RHK six-contact sample puck with the interior shelf mechanically removed to hold a hand-coiled thoriated tungsten filament for electron-beam heating. The crystals were put into a custom UHV preparatory chamber equipped with AES, XPS, ion sputtering, and a Residual Gas Analyzer (RGA). The chamber has a base pressure of $\leq 1.0 \times 10^{-10}$ torr. The crystal surfaces were cleaned by cycling between Ar^+ ion sputtering for 30 min and annealing at 2100 K for 10 min. The surface temperature was monitored with an infrared pyrometer mounted outside of the UHV chamber.

All scanning tunneling microscopy (STM) images were taken at room temperature using an RHK Variable Temperature Beetle-style STM kept in an adjoining UHV chamber with a base pressure of 5.0×10^{-11} torr. Mechanically cut Pt/Ir ($0.8_{Pt}/0.2_{Ir}$) was used for the STM tip and no additional conditioning or sharpening of the tip was performed. STM measurements were performed in constant-current mode. No appreciable bias dependence was observed in the STM images.

For the AES kinetic measurements, native oxide layer was grown by exposure to atmosphere following the aforementioned cleaning methods in UHV. To study structural evolution of the oxidized Nb(100) surface, in situ oxygen exposure was performed while the crystal was in the STM stage by introducing ultra-high purity oxygen gas to the UHV chamber through a variable leak valve. The crystal was held at room temperature during exposure, and the STM tip was retracted out of tunneling range.

3. Results and discussion

STM images of Nb(100) and Nb(111) after preparation are shown in Fig. 1. Despite heating the Nb(111) surface for more than 3 h at 2100 K, and with a clean AES spectra, only disordered clusters were observed in the STM images (Fig. 1A). While these clusters do have some internal structure, there is no obvious long-range order present on the surface. The Nb(100) crystal, however, was prepared in the same manner and regular (3 × 1)-O ladders covered the crystal surface. As the only difference between the two crystals is the orientation of the surface atoms, the surface geometry of the Nb crystal must play a significant role in the ordering of NbO. We note that niobium is a classic bcc crystal with a bulk lattice parameter of 330.04 pm. The (111) plane, therefore, has an interatomic distance of 466.7 pm, while the spacing in the (100) plane is equal to the bulk lattice parameter of 330.04 pm. The (111) face, therefore, has a more open crystal structure in which the top 3 layers of atoms are exposed, as shown in the inset of Fig. 1A. This results in surface Nb atoms being undercoordinated. Fully coordinated surface atoms are energetically favored, and the surface reconstructs and binds O to achieve full coordination. It was expected that long annealing times at temperatures in which surface atoms can overcome the energetic barrier to move to equivalent binding sites on the surface would improve long-range order; this was not observed, however, on Nb(111). In contrast, the Nb(100) face is more closely packed and exposes only the first two layers of Nb atoms (Fig. 1B). As a result, Nb(100) exhibits more long-range order of the Nb($n \times 1$)-O superlattice on Nb(100).

Because Nb(100) is a more well-defined surface than Nb(111) following UHV surface preparation, oxygen dissolution on oxidic Nb

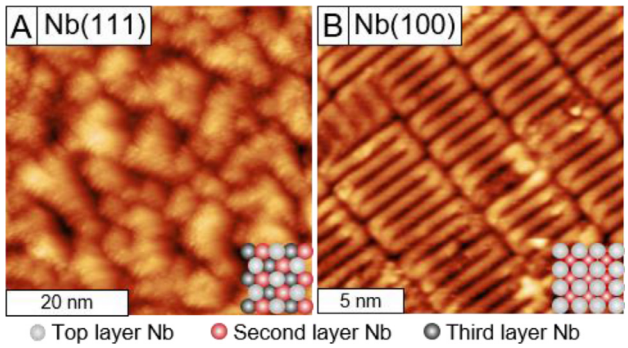

Fig. 1. STM images show surface crystallographic orientation effects on NbO surface structure. (A) $V = -0.5$ V, $I = -0.1$ nA. Nb(111) presents disordered oxide domains with no long-range order due to the open nature of the Nb(111) plane; (B) $V = -0.5$ V, $I = -19$ pA. Nb(100) presents highly-ordered ($n \times 1$)-O superlattices due to the closely-packed Nb(100) plane.

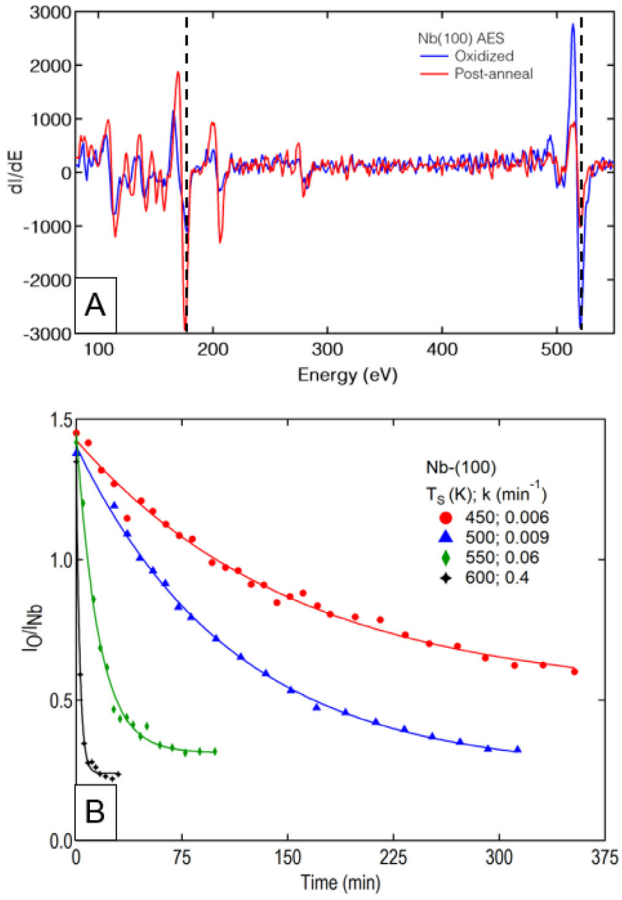

Fig. 2. (A) AES spectra before and after annealing Nb(100) at 600 K. Nb peak at 169 eV, O peak at 519 eV; (B) Ratio of O/Nb current intensity, I_O/I_{Nb}, vs. anneal length for various T_S.

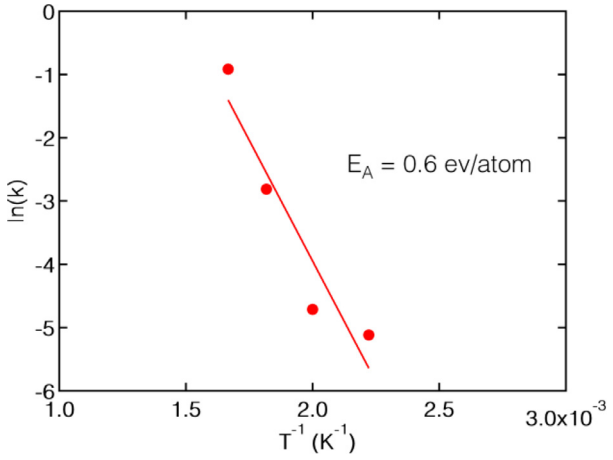

Fig. 3. Arrhenius plot created using the calculated rate constants from the dissolution trials in Fig. 2. An activation energy for oxygen dissolution of 0.6 eV/atom was calculated.

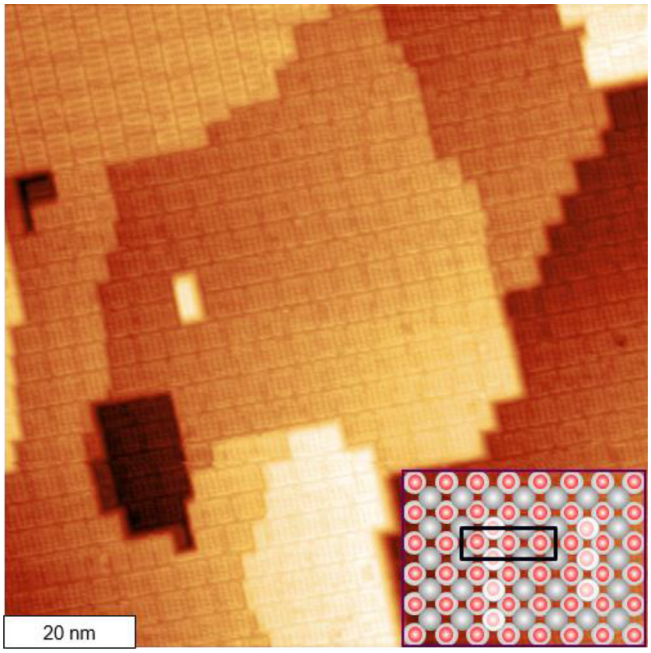

Fig. 4. UHV-STM image ($V = -0.5$ V, $I = -19$ pA) of the Nb(100) surface after Ar-ion sputtering and annealing at 1700 K with (3 × 1)-O schematic inset. Large, flat terraces displaying the (3 × 1)-O superlattice populate the entirety of the Nb(100) crystal.

phases was studied utilizing the Nb(100) crystal. Fig. 2A shows AES spectra of the Nb(100) crystal before (blue) and after (red) annealing (sample temperature, T_S) with the native oxide layer present to promote oxygen dissolution into the bulk metal. The principle Nb AES peak is at 169 eV while the O peak is at 519 eV. Following annealing, there is a significant decrease in the O peak at 519 eV and an increase in the Nb peak intensity at 169 eV. The room temperature O/Nb current intensity ratio (I_O/I_{Nb}) was observed to plateau at ≈ 0.2.

In order to determine the activation energy (E_A) for oxygen dissolution into the bulk, the crystal was annealed at T_S = 450, 500, 550, and 600 K until the I_O/I_{Nb} value plateaued. As shown in Fig. 2B, T_S = 450 K I_O/I_{Nb} stabilized after 350 min with I_O/I_{Nb} = 0.60, T_S = 500 K after 300 min with I_O/I_{Nb} = 0.32, T_S = 550 K after 100 min with I_O/I_{Nb} = 0.31, and T_S = 600 K after 25 min with I_O/I_{Nb} = 0.22. For T_S > 600 K, there was rapid oxygen dissolution, and while a final I_O/I_{Nb} = 0.22 was determined, sequential I_O/I_{Nb} values could not be obtained. Not only did lower T_S result in longer annealing times before I_O/I_{Nb} stabilized, but the amount of oxygen remaining on the surface was higher for lower T_S. This suggests that not only is the rate of oxygen dissolution dependent on T_S, but the oxidic phase present on the surface is in part determined by T_S. The activation energy, E_A, for O dissolution was determined to be 0.6 eV/atom (Fig. 3). Previous work has indicated an E_A for oxygen removal, either *via* evaporation or surface-bulk diffusion, to be 0.74 eV/atom [20], and is in agreement with our experimentally determined E_A of 0.6 eV/atom.

Following sputtering and annealing, Nb(100) was placed into the UHV-STM, and the (3 × 1)-O ladder structure was observed on all terraces of the Nb(100) surface, as shown in Fig. 4. Further analysis of the parallel rows of (3 × 1)-O ladders shows that while the spacing between the ladders is a constant in the (3 × 1)-O structure, the widths of the ladders are not constant, and are rather distributed in a range of sizes. Fig. 5A shows the statistical distribution of the periodic widths of the (3 × 1)-O ladder structures in units of the surface layer Nb-to-Nb interatomic distance (0.31 nm) [41]. The distribution of the ladder widths is symmetric and centered around 10 Nb atoms. This is consistent with previously reported statistical analysis of the periodic widths of the (3 × 1)-O ladder widths on Nb(100) [34,36].

To characterize the structural evolution of the ladder structures as a result of oxygen dissolution, the (3 × 1)-O ladders were exposed to oxygen gas and annealed at 725 K to promote oxygen dissolution but not regrow the ladder structures. This allowed us to make comparisons between the thermal annealed Nb(100) surface following oxygen dissolution to the initial, pristine Nb(100) (3 × 1)-O surface. The surface comprised of ladder structures in Fig. 5A was exposed to 3.6 L O_2 at T_S = 300 K. This resulted in the chemisorption of oxygen atoms (O_{ad})

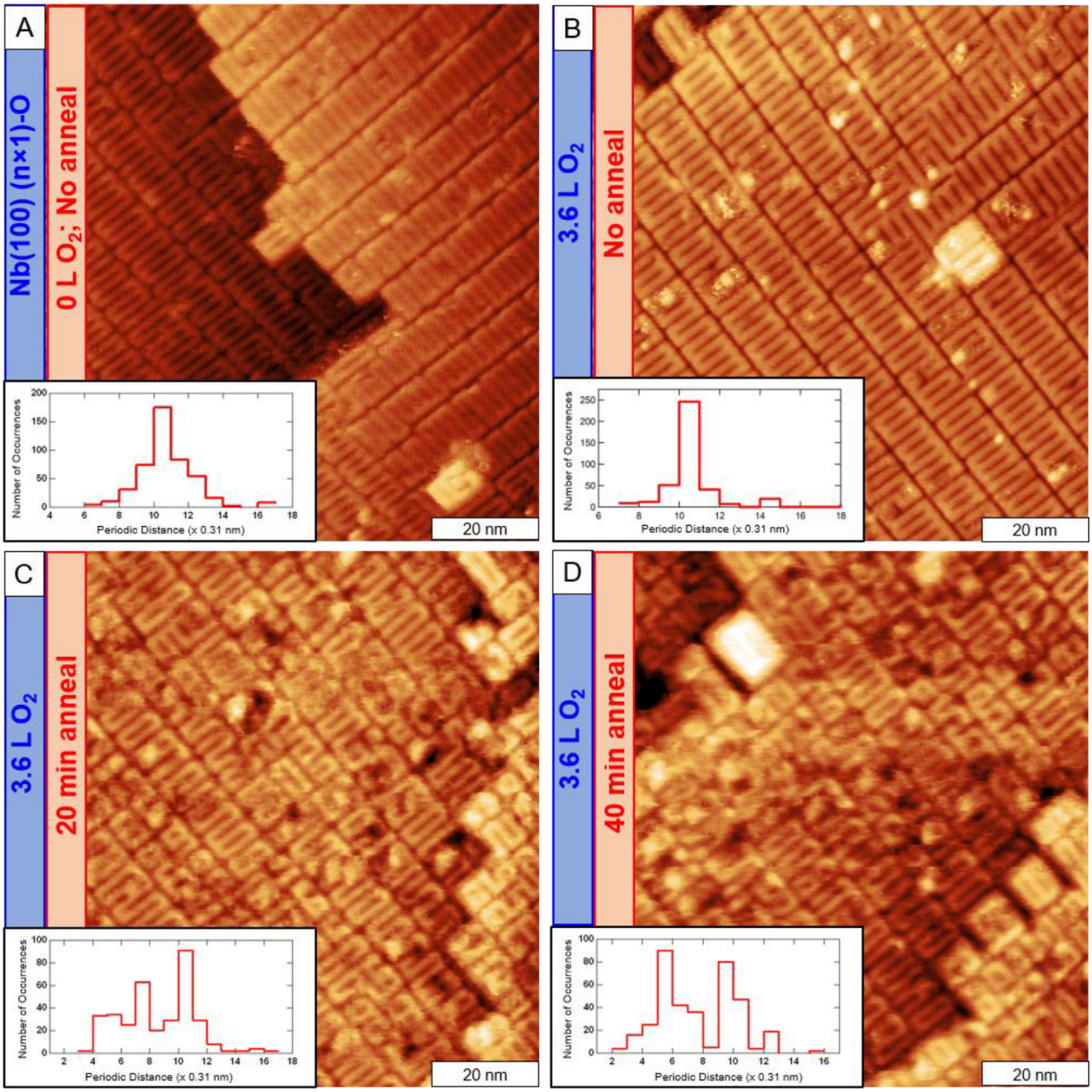

Fig. 5. STM images of the Nb(100) (3 × 1)-O surface after two subsequent doses of 3.6 L of oxygen gas at T_C = 300 K and subsequent annealing at 725 K. (A) Pristine (3 × 1)-O surface and ladder width histogram; (B) (3 × 1)-O surface with chemisorbed O_{ad} following a 3.6 L O_2 exposure with no anneal; (C) (3 × 1)-O surface with 3.6 L O_2 annealed at 725 K for 20 min total and ladder width histogram; (D) (3 × 1)-O surface with 3.6 L O_2 annealed at 725 K for 40 min total and ladder width histogram. Imaging conditions: (A) $V = -0.5$ V, $I = -19$ pA; (B) $V = -0.5$ V, $I = -18$ pA; (C) $V = -0.51$ V, $I = -19$ pA (D) $V = -0.51$ V, $I = -18$ pA.

across the NbO surface oxide with no incorporation of oxygen into the ladder structure nor evolution of the underlying ladder structure, as seen in Fig. 5B. Statistical analysis was performed on the ladder structures in Fig. 5B to confirm that the underlying surface structure of the ladders had not been altered, and similar to the distribution of ladder widths in Fig. 5A, the majority of ladders were 10 Nb atoms wide. After confirming that the chemisorption of O_{ad} did not perturb the underlying (3 × 1)-O ladder structure, the surface was annealed at T_S = 725 K for 20 min to promote the dissolution of chemisorbed oxygen through the ladder structures into the Nb bulk as shown in Fig. 5C. The ladder structures, while still present, have begun to break apart as a result of oxygen dissolution into the bulk of the Nb crystal. The ladders are now interrupted with dark pits on the surface, consistent with more extensive oxidation, and ladder rungs are segmented into smaller ladder fragments. Visually, there is a marked decrease in overall ladder domain order compared to the pristine ladder surface in Fig. 5A. A histogram of the periodic ladder lengths, shown in the histogram inset of Fig. 5C, confirms the evolution of the ladder widths, with a larger portion of the Nb surface comprised of narrower ladder features. While there are still 10 Nb atom wide ladders present on the surface, a significant portion of the ladders have been disrupted by the oxygen dissolution and a noticeable increase in narrower ladder widths are observed.

Following the 20 min anneal at T_S = 725 K, the surface was annealed for an additional 20 min, resulting in a total anneal time of 40 min. Fig. 5D shows the continued surface evolution following the 40 min total anneal at T_S = 725 K. In addition to the dark pits consistent with further surface oxidation as was shown in Fig. 5C, there are small areas where no ladder pattern is discernable. Additionally, there is an increase in the occurrence of narrow ladder widths compared to

Fig. 5A–C, as seen in the histogram inset of Fig. 5D. The most frequent ladder width in Fig. 5D has also shifted from 10 Nb atoms to 9, consistent with continual surface evolution as the oxygen dissolution disrupts the original pristine ladders as it diffuses into the bulk. It is interesting to note the frequent occurrence of 5 Nb atoms in this histogram inset of Fig. 5D, which is half of the unperturbed ladder length of 10 Nb atoms. This could indicate a preferred location for O_{ad} penetration into the bulk at the center point of the existing ladder rungs. Following the extensive anneal at $T_S = 725$ K, the surface was annealed further above $T_S = 900$ K, and the pristine (3 × 1)-O surface was restored.

These surface reconstructions provide the first detailed visualization of changes to the Nb(n × 1)-O superlattice on Nb(100) that result from chemisorbed O_{ad} dissolving into the bulk. This is important for understanding the changes that occur at the oxide/metal interface during mild bake treatments to improve SRF cavity performance, contaminant and dopant incorporation into the Nb bulk, and the growth of thin films on oxide covered niobium to improve SRF performance with next generation superconducting alloys such as Nb_3Sn. Future studies will combine these results with first principles calculations to develop an atomic scale model for oxygen dissolution and mass transport through the Nb(100) (3 × 1)-O ladder structures.

4. Conclusion

In order to elucidate the energetics of oxygen dissolution through relevant (3 × 1)-O ladder structures on Nb(100) and subsequent atomic-scale structural evolution as a result of oxygen dissolution, the (3 × 1)-O ladder structure on Nb(100) was studied with AES and STM following thermal annealing to provide ensemble chemical and local structural information of the Nb surface. The (111) and (100) faces of Nb were used as model systems to investigate differences in surface oxide ordering, and it was discovered that the Nb(100) surface forms (3 × 1)-O ladder structures with large, ordered domains while the Nb (111) surface oxide does not form long-range order despite extended high temperature thermal annealing. Surface reconstructions of the Nb (100) (3 × 1)-O surface were observed as a result of oxygen dissolution into the bulk, and these results provide a detailed visualization of the changing structure of the oxide/metal interface during oxygen dissolution promoted by mild heat treatments of the niobium metal. In addition, the rate for oxygen dissolution was determined across a range of temperatures yielding an activation energy for oxygen dissolution of 0.6 eV/atom. This work provides real-space structural information regarding the complex surface evolution of Nb oxide as a function of thermal annealing, and has significant implications for actual SRF cavity fabrication processes. The importance of Nb oxide structure and chemical composition dictates the efficacy of beneficial dopant incorporation, the formation of high Q thin films such as Nb_3Sn, and the overall performance of SRF cavities under operating conditions. By increasing our understanding of the fundamental energetics and structural evolution of the Nb(100) (3 × 1)-O surface during oxygen dissolution, the opportunity to optimize Nb SRF cavity fabrication for increased particle accelerator facility performance may be realized.

Acknowledgments

This work was supported by the U.S. National Science Foundation under Award PHY-1549132, the Center for Bright Beams. Preliminary work was supported by the U.S. National Science Foundation under Award PHY-1535639. R.D.V. thanks Fermi National Accelerator Laboratory and The University of Chicago for partial fellowship support during this work.

References

[1] Hasan Padamsee, RF Superconductivity, 159 Wiley-VCH, Weinheim, 2009.
[2] D.C. Ford, L.D. Cooley, D.N. Seidman, Suppression of Hydride Precipitates in Niobium Superconducting Radio-Frequency Cavities, Supercond. Sci. Technol. 26 (2013) 105003.
[3] D.C. Ford, L.D. Cooley, D.N. Seidman, First-principles calculations of niobium hydride formation in superconducting radio-frequency cavities, Supercond. Sci. Technol. 26 (2013) 095002.
[4] F. Barkov, A. Romanenko, Y. Trenikhina, A. Grassellino, Precipitation of Hydrides in High Purity Niobium after Different Treatments, J. Appl. Phys. 114 (2013) 164904.
[5] R. Tao, A. Romanenko, L.D. Cooley, R.F. Klie, Low temperature study of structural phase transitions in niobium hydrides, J. Appl. Phys. 114 (2013) 044306.
[6] A. Romanenko, F. Barkov, L.D. Cooley, A. Grassellino, Proximity breakdown of hydrides in superconducting niobium cavities, Supercond. Sci. Technol. 26 (2013) 035003.
[7] A. Romanenko, A. Grassellino, F. Barkov, J.P. Ozelis, Effect of mild baking on superconducting niobium cavities investigated by sequential nanoremoval, Phys. Rev. Spec. Top. - Accel. Beams. 16 (2013) 012001.
[8] A. Grassellino, A. Romanenko, D. Sergatskov, O. Melnychuk, Y. Trenikhina, A. Crawford, A. Rowe, M. Wong, T. Khabiboulline, F. Barkov, Nitrogen and argon doping of niobium for superconducting radio frequency cavities: a pathway to highly efficient accelerating structures, Supercond. Sci. Technol. 26 (2013) 102001.
[9] G. Ciovati, Review of the frontier workshop and Q-slope results, Phys. C Supercond. 441 (2006) 44–50.
[10] F. Barkov, A. Romanenko, Y. Trenikhina, A. Grassellino, Precipitation of hydrides in high purity niobium after different treatments, J. Appl. Phys. 114 (2013) 164904.
[11] F. Barkov, A. Romanenko, A. Grassellino, Direct observation of hydrides formation in cavity-grade niobium, Phys. Rev. Spec. Top. - Accel. Beams. 15 (2012) 122001.
[12] P. Garg, S. Balachandran, I. Adlakha, P.J. Lee, T.R. Bieler, K.N. Solanki, Revealing the role of nitrogen on hydride nucleation and stability in pure niobium using first principles calculations, Supercond. Sci. Technol. 31 (2018) 115007.
[13] Y. Trenikhina, A. Grassellino, O. Melnychuk, A. Romanenko, Characterization of Nitrogen Doping Recipes for the Nb SRF Cavities, SRF2015 MOPB055 (2015).
[14] S. Posen, M. Liepe, Advances in development of Nb3Sn superconducting radio-frequency cavities, Phys. Rev. Spec. Top. - Accel. Beams. 17 (2014) 112001.
[15] G. Arnolds, D. Proch, Measurement on a Nb3Sn structure for linear accelerator application, IEEE Trans. Magn. 13 (1977) 500–503.
[16] P. Kneisel, O. Stoltz, J. Halbritter, Measurements of superconducting Nb3Sn cavities in the GHz range, IEEE Trans. Magn. 15 (1979) 21–24.
[17] S. Posen, D.L. Hall, Nb3Sn superconducting radiofrequency cavities: fabrication, results, properties, and prospects, Supercond. Sci. Technol. 30 (2017) 033004.
[18] R. Franchy, T.U. Bartke, P. Gassmann, The interaction of oxygen with Nb(110) at 300, 80 and 20 K, Surf. Sci. 366 (1996) 60–70.
[19] H.H. Farrell, M. Strongin, The interaction of oxygen and nitrogen with the niobium (100) surface: I. Morphology, Surf. Sci. 38 (1973) 18–30.
[20] H.H. Farrell, H.S. Isaacs, M. Strongin, The interaction of oxygen and nitrogen with the niobium (100) surface: II. Reaction kinetics, Surf. Sci. 38 (1973) 31–52.
[21] P.H. Dawson, Wing-Cheung Tam, The interaction of oxygen with polycrystalline niobium studied using aes and low-energy sims, Surf. Sci. 81 (1979) 464–478.
[22] K.H. Rieder, On the interaction of oxygen with Nb(110) and Nb(750), Appl. Surf. Sci. 4 (1980) 183–195.
[23] Z.P. Hu, Y.P. Li, M.R. Ji, J.X. Wu, The interaction of oxygen with niobium studied by XPS and UPS, Solid State Commun 71 (1989) 849–852.
[24] J.M. Sanz, S. Hofmann, Auger electron spectroscopy and X-ray photoelectron spectroscopy studies of the oxidation of polycrystalline tantalum and niobium at room temperature and low oxygen pressures, J. Common Met. 92 (1983) 317–327.
[25] I. Lindau, W.E. Spicer, Oxidation of Nb as studied by the uv-photoemission technique, J. Appl. Phys. 45 (1974) 3720–3725.
[26] Y. Wang, X. Wei, Z. Tian, Y. Cao, R. Zhai, T. Ushikubo, K. Sato, S. Zhuang, AES An, UPS and HREELS study of the oxidation and reaction of Nb(110), Surf. Sci. 372 (1997) L285–L290.
[27] R.A. Pasternak, B. Evans, Adsorption, Absorption, and Degassing in the Oxygen-Niobium System at Very Low Pressure, J. Electrochem. Soc. 114 (1967) 452–457.
[28] G. Hörz, Mechanisms and kinetics of absorption and desorption reactions in systems of refractory metals with nitrogen, oxygen or carbon, Metall. Trans. 3 (1972) 3069–3076.
[29] W.-S. Lo, H.-H. Chen, T.-S. Chien, C.-C. Tsan, B.-S. Fang, OXIDATION OF Nb(001) STUDIED BY HIGH-RESOLUTION CORE-LEVEL PHOTOEMISSION, Surf. Rev. Lett. 04 (1997) 651–654.
[30] B.R. King, H.C. Patel, D.A. Gulino, B.J. Tatarchuk, Kinetic measurements of oxygen dissolution into niobium substrates: In situ X-ray photoelectron spectroscopy studies, Thin Solid Films 192 (1990) 351–369.
[31] I. Arfaoui, C. Guillot, J. Cousty, C. Antoine, Evidence for a large enrichment of interstitial oxygen atoms in the nanometer-thick metal layer at the NbO/Nb (110) interface, J. Appl. Phys. 91 (2002) 9319–9323.
[32] C. Sürgers, M. Schöck, H. v. Löhneysen, Oxygen-induced surface structure of Nb (110), Surf. Sci. 471 (2001) 209–218.
[33] Y. Uehara, T. Fujita, M. Iwami, S. Ushioda, Single NbO nano-crystal formation on low temperature annealed Nb(001) surface, Surf. Sci. 472 (2001) 59–62.
[34] Y. Li, B. An, X. Xu, S. Fukuyama, K. Yokogawa, M. Yoshimura, Surface structure of niobium-dioxide overlayer on niobium(100) identified by scanning tunneling microscopy, J. Appl. Phys. 89 (2001) 4772–4776.
[35] R. Pantel, M. Bujor, J. Bardolle, Continuous measurement of surface potential variations during oxygen adsorption on the (100), (110) and (111) faces of niobium using mirror electron microscope, Surf. Sci. 62 (1977) 589–609.
[36] S. Usami, N. Tominaga, T. Nakajima, AES-LEED study of adsorption of common

gases on the (100) planes of W and Nb, Vacuum 27 (1977) 11–16.
[37] A. Daccà, G. Gemme, L. Mattera, R. Parodi, XPS analysis of the surface composition of niobium for superconducting RF cavities, Appl. Surf. Sci. 126 (1998) 219–230.
[38] L.H. Rovner, A. Drowart, F. Degreve, J. Drowart, Air Force Materials Laboratory Technical Report AFML-TR-68-200, July, 1968.
[39] N. Greenwood, A. Earnshaw, Chemistry of the Elements, 2nd ed., Butterworth-Heinemen, Oxford, 1997.
[40] H. Oechsner, J. Giber, H.J. Füßer, A. Darlinski, Phase transition and oxide dissolution processes in vacuum-annealed anodic Nb2O5/Nb systems, Thin Solid Films 124 (1985) 199–210.
[41] B. An, S. Fukuyama, K. Yokogawa, M. Yoshimura, Surface structures of clean and oxidized Nb(100) by LEED, AES, and STM, Phys. Rev. B. 68 (2003) 115423.
[42] Y. Li, B. An, S. Fukuyama, K. Yokogawa, M. Yoshimura, Surface oxidation of a Nb (100) single crystal by scanning tunneling microscopy, Mater. Charact. 48 (2002) 163–167.
[43] A.S. Razinkin, M.V. Kuznetsov, Scanning tunneling microscopy (STM) of low-dimensional NbO structures on the Nb(110) surface, Phys. Met. Metallogr. 110 (2010) 531–541.
[44] I. Arfaoui, J. Cousty, C. Guillot, A model of the NbOx≈1 nanocrystals tiling a Nb (110) surface annealed in UHV, Surf. Sci. 557 (2004) 119–128.